

HiSST: 4th International Conference on High-Speed Vehicle Science Technology 22 -26 September 2025, Tours, France



Numerical Simulations of a Continuous Detonation Ramjet Fueled by Ethylene

Rui Li¹, Jinglei Xu², Kunyuan Zhang³

Abstract

This study numerically investigates the performance of a non-premixed continuous detonation ramjet fueled by ethylene. The design point is set to a flight Mach number of five at the flight height of 20 km, and the fuel is pumped into the cavity-based combustor at a total pressure of 1 MPa and a total temperature of 300 K. After the ignition, the working frequency is stabilized at 5787 Hz, and the model reaches a mass flow rate of 0.52 kg·s⁻¹. In the entire operating process, the reverse shock wave occupies one-third of the axial length of the isolator, and the strength of the trailing shock wave weakens along the flow path. At the combustor exit, RMSD $_{\theta}$ and Mach number are separately equal to 6.57° and 1.04, indicating that the flow fluctuations are moderate and the nozzle converging section is unnecessary. These features imply that the design of the compression system and the exhaust system for this engine outline can still follow the methods in steady flows to some extent. In addition, the increase in the total temperature is 1503 K, demonstrating the superiority of detonation in the energy addition to the high-speed mainstream.

Keywords: coupling effects, cavity-based continuous detonation combustor, aerodynamic performance

Nomenclature

U – Conserved quantity vector
t – Time, s
E, F, G – Inviscid flux components
E_v, F_v, G_v – Viscous flux components
Q – Chemical reaction source term
u, v, w – Velocity components, m·s⁻¹
e – Internal energy per unit volume, J·m⁻³
h – Enthalpy per unit mass, J·kq⁻¹

 C_p – Constant-pressure specific heat, $J \cdot kg^{\text{-}1} \cdot K^{\text{-}1}$ R_u – Universal gas constant, $J \cdot kg^{\text{-}1} \cdot K^{\text{-}1}$ Mo – Molar weight RMSD0 – RMSD of flow angle to the axis, ° Mach – Mach number \dot{m} – Mass flow rate, $kg \cdot s^{\text{-}1}$ ρ – Density, $kg \cdot m^{\text{-}3}$

1. Introduction

In comparison with the conventional aero-engines, the propulsion systems relying on detonation show more benefits in the thermodynamic efficiency, due to the abrupt increments in the post-detonation parameters, the limited entropy production, and the ultra-fast heat release. Differing from the Brayton cycle, the Zeldovich-von Neumann-Doring cycle with the same initial state for the detonation has an extra spike in the pressure-specific volume diagram, bringing a net total pressure gain and an increase in the available energy [1]. To effectively utilize the flow features, such as the propagation velocity at the order of kilometers per second and the tight coupling effects between the combustion waves and shock waves, the continuous detonation engines (RDEs) are most widely investigated. After a single ignition, the detonation waves continuously propagate in the circumferential direction, generating

HiSST-2025-XXXX Page | 1
Numerical Simulations of a Continuous Detonation Engine Fueled by Ethylene Copyright © 2025 by author(s)

¹ Nanjing University of Aeronautics and Astronautics, Nanjing City, Jiangsu Province, China, ruili@nuaa.edu.cn

² Nanjing University of Aeronautics and Astronautics, Nanjing City, Jiangsu Province, China, xujl@nuaa.edu.cn

³ Nanjing University of Aeronautics and Astronautics, Nanjing City, Jiangsu Province, China, zkype@nuaa.edu.cn

positive thrust in a complete cycle [2-5]. It is promising that the RDEs may bring technical breakthroughs to high-speed flight vehicles.

With effective fuel residence time, relatively compact geometrical parameters, and high impulses, the RDEs are capable of fulfilling the increasing demands of low-cost fast-reaching capability. Till now, the integration possibility of RDEs into the ramjets has been discussed in several published works. Braun et al. [6] used to create an air-breathing RDE cycle analysis tool that contains a steady compression system, an annular combustor, and a nozzle. The results showed that an air-breathing RDE can reach the flight Mach number of five. Ivanov et al. [7] directly conducted hot-fire tests of an RDE ramjet, demonstrating that continuous detonation mode can also be obtained at some low flight Mach numbers. Frolov et al. [8] realized the hot-fire tests of the RDE ramjet model with flight Mach numbers ranging from 5 to 8, where two states are observed: continuous detonation mode and longitudinally pulsating detonation mode. Dubrovskii et al. [9] numerically simulated a ramjet RDE model at a flight Mach number of five and an altitude of 20 km, where the positively effective thrust was captured. These findings largely enhance the researchers' faith in further developing an RDE operating successfully at the ram-compression state over a long time duration.

As revealed in the previous studies [10, 11], the propagation stability boundary in the annular RDE combustor should be properly treated and controlled. One way is to reduce the inner cylinder radius and broaden the channel width in the annular RDEs, and its limiting case is the hollow RDE combustor [12, 13]. However, the hollow RDE combustor cannot always have a satisfying chamber pressure. The compromise is the cavity-based RDE combustor, which effectively generates the wide ignition points [14, 15].

Based on the aforementioned status, this study mainly focuses on the numerical simulations of a non-premixed RDE combustor with a mixed compression system at a flight Mach number of five. First, the governing equations in this problem are introduced. Second, the geometrical details of this RDE are presented. Third, the aerodynamic performance and dynamic responses of this RDE after ignition are discussed.

2. Governing equations

Because the coupling effects among the compression system, isolator, and combustor are related to multiple discontinuities and intense exothermic reactions, the governing equations for this type of flow are the transient Reynolds-averaged Navier-Stokes equations along with the energy and species transportation equations [16], which are written as follows

$$\frac{\partial U}{\partial t} + \frac{\partial (E - E_v)}{\partial x} + \frac{\partial (F - F_v)}{\partial y} + \frac{\partial (G - G_v)}{\partial z} = Q \tag{1}$$

where U is the conserved quantity vector; E, F, and G are the inviscid flux components in the orthogonal coordinate system; E_v , F_v , and G_v , respectively, denote the viscous fluxes in the x, y, and z directions; Q accounts for the chemical reaction source term of the ethylene/air mixture.

The total energy per unit volume e appearing in U is expressed by

$$e = \sum \rho_i h_i - p + \frac{1}{2} \rho (u^2 + v^2 + w^2)$$
 (2)

$$h_i(T) = \int_{T_0}^T C_{pi}(T) dT + h_i^0$$
 (3)

where h_i and C_{pi} are the specific enthalpy and constant-pressure specific heat of the ith species. The mixed static pressure is determined by the ideal gas state equation

$$p = \sum \rho_i \frac{R_u}{Mo_i} T \tag{4}$$

where R_u , M_{oi} , and T denote the universal gas constant, molar weight of the ith species, and static temperature. Meanwhile, the mixed density is made up of all the partial densities as follows

$$\rho = \sum \rho_i \tag{5}$$

To precisely capture the viscous effects, Sutherland's law is adopted to describe the laminar part of viscosity, and the k- ω SST turbulence model is utilized to calculate the turbulent part of viscosity [17].

Based on the finite volume technique, the governing equations are discretized in the spatial domain for the following simulations. The inviscid fluxes through the cell faces are approximated by Roe's scheme along with the third-order MUSCL interpolation, and the viscous terms are calculated by the central differential method. As for the time integration, a second-order implicit scheme is adopted.

3. Three-Dimensional Full-Scale Model Description

As shown in Fig.1, the three-dimensional computational domain consists of a hypersonic compression system, a diverging annular isolator, and a cavity-based continuous detonation combustor. The designed point is set to Mach 5 at a flight height of 20 km. The external compression section is a part of the cone with a length of 125 mm, and the rest of the cone, along with the straight cowl, performs as the internal compression section. The isolator with a diverging angle of 3° is used to prevent the upstream propagation of the reverse shock wave. In addition, there are 30 square injectors placed equidistantly in the circumferential direction at the fore-wall edge of the cavity with a deflection angle of 60°. The gaseous ethylene serves as the fuel, which is pumped into the combustor at a total pressure of 1 MPa and a total temperature of 300 K. The depth and length of the annular cavity are 3 mm and 30 mm, which are responsible for the flame holding. Furthermore, the complete combustion is almost achieved in the straight section with a length of 30 mm downstream of the cavity. To capture the dynamic responses of pressure along the flowpath, the monitoring points are set on a cylindrical surface with a radius of 32.9 mm, and their coordinates are shown in Tab.1 in the premise that the coordinate origin is the cone vertex.

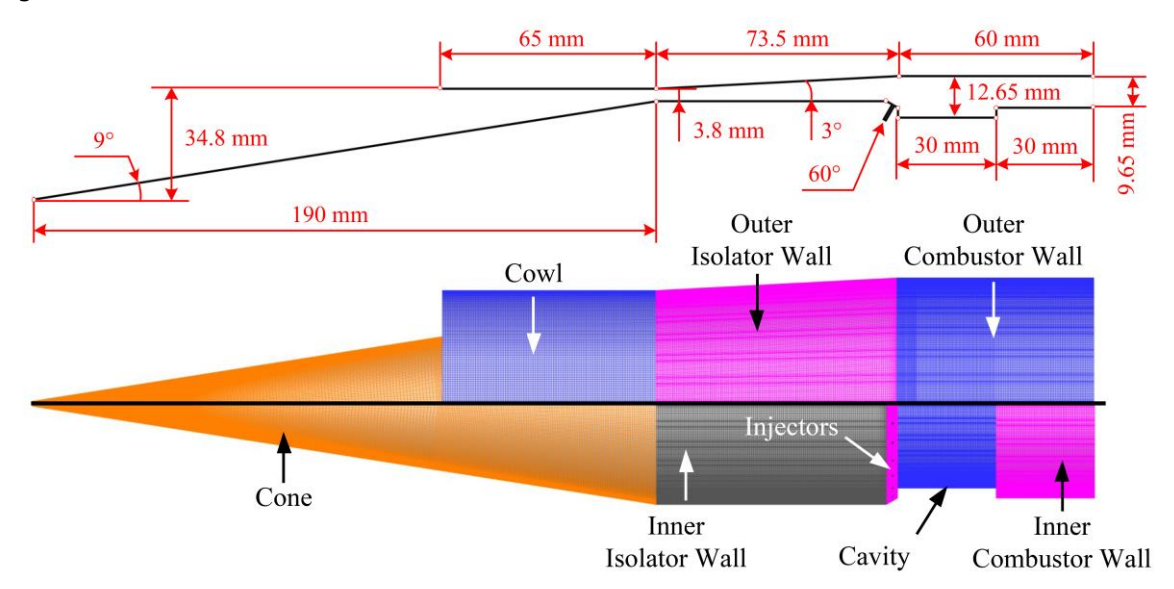


Fig 1. Configuration and grids of a cavity-based continuous detonation combustor coupled with a hypersonic inlet.

Points	x, mm	y, mm
А	240.00	32.90
В	250.00	32.90
С	260.00	32.90
D	278.00	32.90
E	293.00	32.90
F	308.00	32.90

Table 1. Locations of the monitoring points

4. Results and Discussions

The morphologies of the detonation structures are illustrated in Fig.2. Here, the three-dimensional characteristics are represented by the isosurface of the stochiometric mass fraction of the fuel and colored by the static temperature, and the two-dimensional features are exhibited by the unwrapped pressure distributions. In the post-detonation region, the maxima of temperature and pressure are approximately 3100 K and 1.3 MPa. It can also be observed that the detonation front is restricted in the annular cavity and its foot steps on the fore-wall edge of the cavity. Under the high-enthalpy inflow condition, the fuel is no longer largely consumed in the detonation phenomena, and the combustion along the contact discontinuity is gradually enhanced. Meanwhile, the reverse shock wave extends into the isolator and roughly occupies one-third of the isolator length, indicating that the diverging isolator in this study has an excellent pressure-resistance capacity. From the Mach number distributions in the meridian plane, the existence of the detonation wave results in the transonic flow parameters in the cavity, which is beneficial for the fuel mixing. The trailing shock wave is almost parallel to the inflow direction, and its strength continuously weakens from the rear-wall edge of the cavity to the combustor exit. The blurring boundary between the pre- and post-shock states at the combustor exit implies that the selected length of the straight section in the combustor is feasible to dampen the flow fluctuations caused by the periodic shock sweeping. In general, the current configuration makes it possible to cut off the influence of the continuous detonation to some extent, and the design of the inlet and exhaust system can still follow the methods and principles of the steady flow.

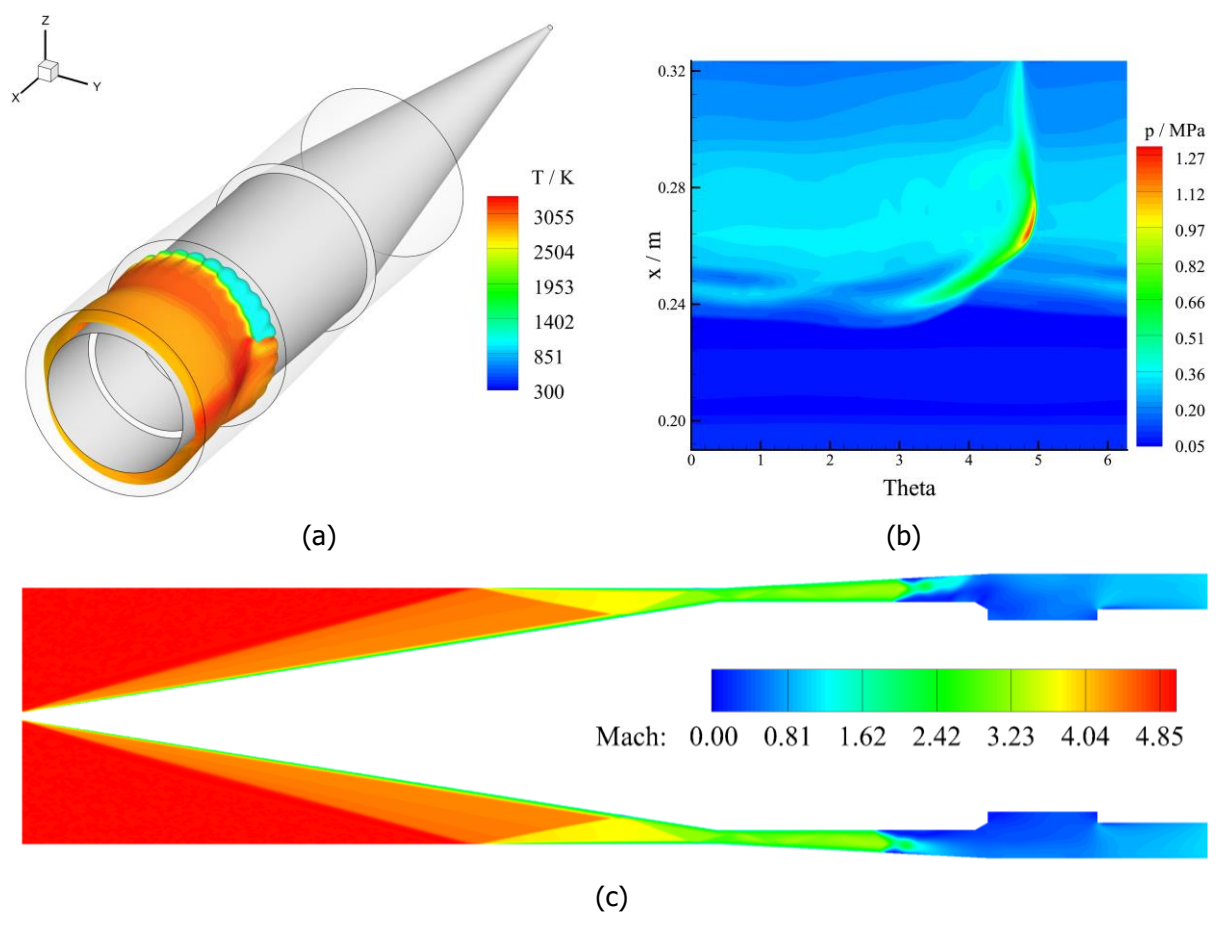


Fig 2. Morphologies of the detonation structures: (a) Three-dimensional characteristics; (b) Unwrapped two-dimensional features from the outer wall; (c) Transient meridian Mach number distributions.

Figure 3 describes the mass fraction distributions of ethylene on the inner wall and the meridian plane at different attack angles without ignition. The region with $Y_{\text{C2H4}} > 0.17$ almost conquers the entire cavity in a relatively steady flowfield without ignition. The outer airflow is hard to enter the recirculation zone filled with ethylene, where the mixing process between the fuel and the oxidants can only be achieved by the shear layers. At three different attack angles, the mass fractions of ethylene along

these shear layers are all close to 0.09, implying that a slightly fuel-rich environment exists on the central ring surface in the cavity. In addition, the forward-face step at the entrance of the straight tube section induces the flow deflection, and the fuel dispersion is strengthened. Because the asymmetric shock waves without ignition still evolve in the straight tube section, the non-uniform domains of ethylene are inevitably enlarged but gradually closer to the stoichiometric conditions.

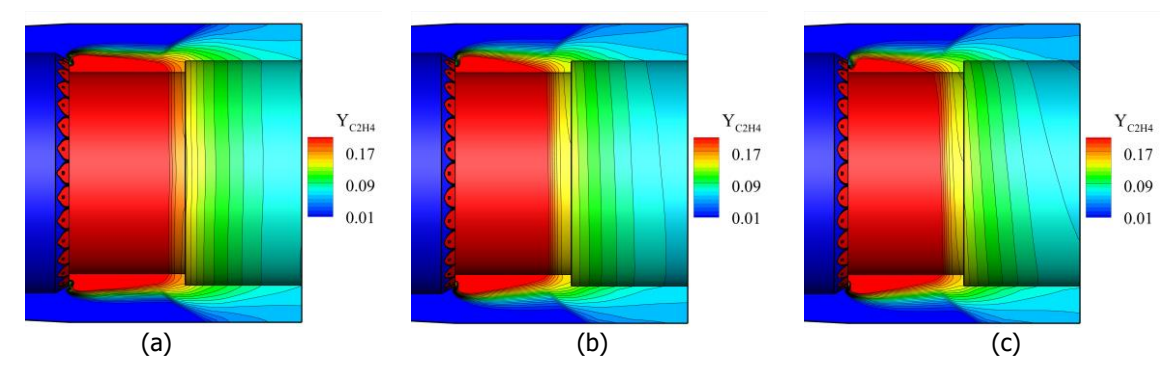


Fig 3. Mass fraction distributions of C2H4 in the side and top views at different attack angles: (a) $AOA = 0^{\circ}$; (b) $AOA = 2^{\circ}$; (c) $AOA = 4^{\circ}$.

The definition of the mixing efficiency is shown below

$$\eta_{mix}(x) = \frac{\iint Y_{C_2H_4}^r \cdot \rho u \cdot dydz}{\iint Y_{C_2H_4} \cdot \rho u \cdot dydz}$$
(6)

where

$$Y_{C_{2}H_{4}}^{r} = \begin{cases} Y_{C_{2}H_{4}}, & Y_{C_{2}H_{4}} < Y_{C_{2}H_{4}}^{stoic} \\ \left(\frac{1 - Y_{C_{2}H_{4}}}{1 - Y_{C_{2}H_{4}}^{stoic}}\right) \cdot Y_{C_{2}H_{4}}^{stoic}, & Y_{C_{2}H_{4}} > Y_{C_{2}H_{4}}^{stoic} \end{cases}$$
(7)

where ρ and u denote the density and velocity component in the x-direction, $Y_{C_2H_4}$ and $Y_{C_2H_4}^r$ denote the total and combustible mass fractions of ethylene, and $Y_{C_2H_4}^{stoic}$ is equal to 0.0637 related to the stoichiometric conditions. As depicted in Fig.4, the mixing efficiency rises axially at three different attack angles. In the range of $x = 270 \sim 290$ mm, the mixing efficiency at AOA = 4° exceeds those at AOA = 0° and AOA = 2° by 0.08 and 0.04, implying that the increase in the non-uniformity can magnify the interactions between the mainstream and the fuel jets in the cavity. In the range of $x = 290 \sim 320$ mm, the discrepancies among the mixing efficiencies at three attack angles are reduced, where the values first rise rapidly and then asymptotically converge to one. It shows that the formation of a converging channel by the aft wall of the cavity and the straight walls regulates the flow and forces the crossstream blending. With the increase in the attack angle, the mixed reactants are more prone to ignition.

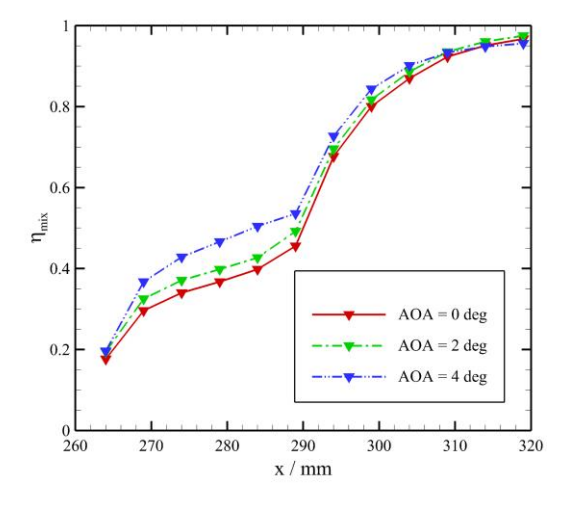
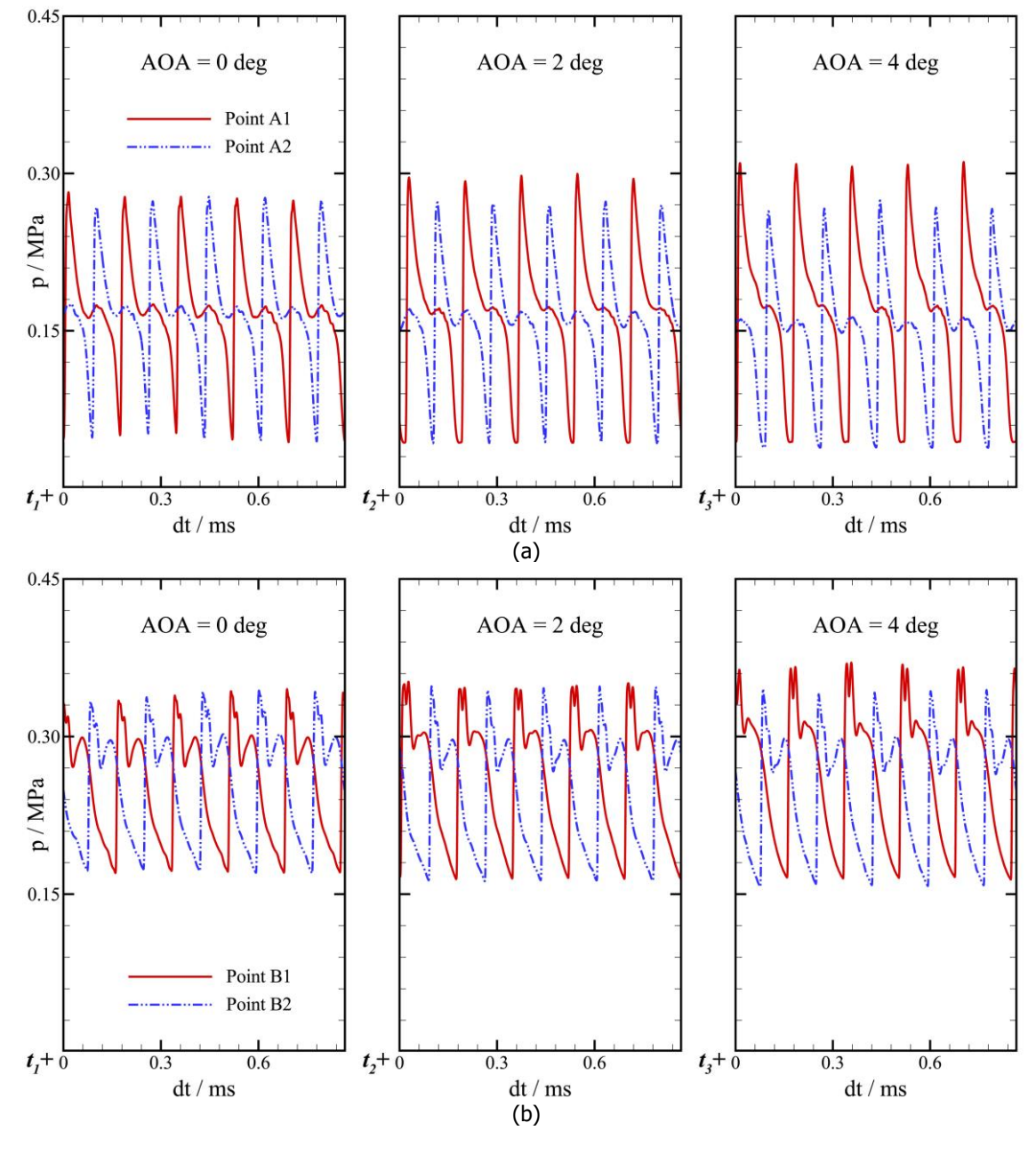


Fig 4. Axial distributions of the mixing efficiencies for the states without ignitions at different attack angles.

As illustrated in Fig.5, the dynamic pressure signals of the monitoring points upstream of the cavity forewall are captured to study the movement of the reverse shock wave system at three different attack angles. Here, points A1 and A2 are continuously disturbed by the reverse shock wave; points B1 and B2 are affected by the triple point where the reverse shock wave, detonation foot, and shear layers intersect; points C1 and C2 are consistently swept by the part of the detonation front penetrating the isolator. Because the points with subscripts "1" and "2" are placed with a circumferential angle difference of 180°, the phase difference of the dynamic pressure is naturally equal to a half cycle. With the increase in the attack angle, the average pressure peaks of points A1, B1, and C1 are, respectively, raised by 11.5%, 7.4%, and 12.7%, while those of points A2, B2, and C2 separately drop by 2.3%, 0.5%, and 8.6%. The underlying reason is that the inflow compression on the windward side is more intense than on the leeward side, leading to the local overpressure of the fuel injector on the windward side. The mass fraction of fuel in the circumferential direction becomes highly non-uniform, and the enlarged chemical heat release on the leeward side promotes the detonation strength asymmetrically. Two pressure peaks of B1 appear in a single cycle at a non-zero attack angle, indicating that some oscillations and bifurcations near the reverse shock waves exist on the leeward sides.



HiSST-2025-XXXX Page | 6
R. Li, J. L. Xu Copyright © 2025 by author(s)

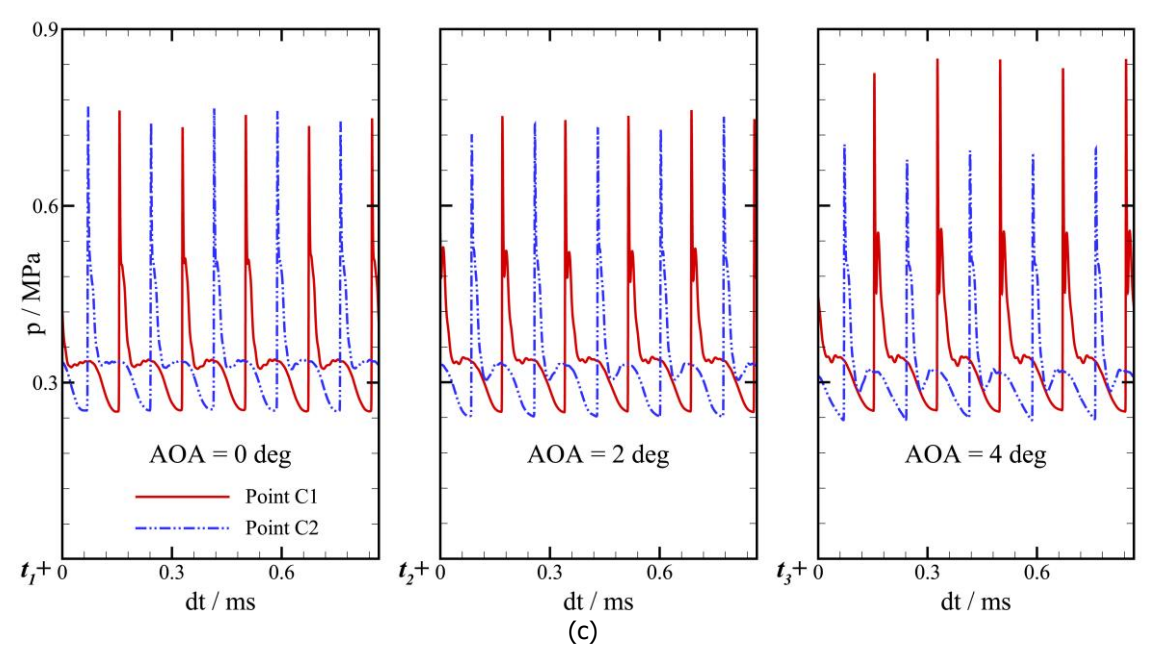
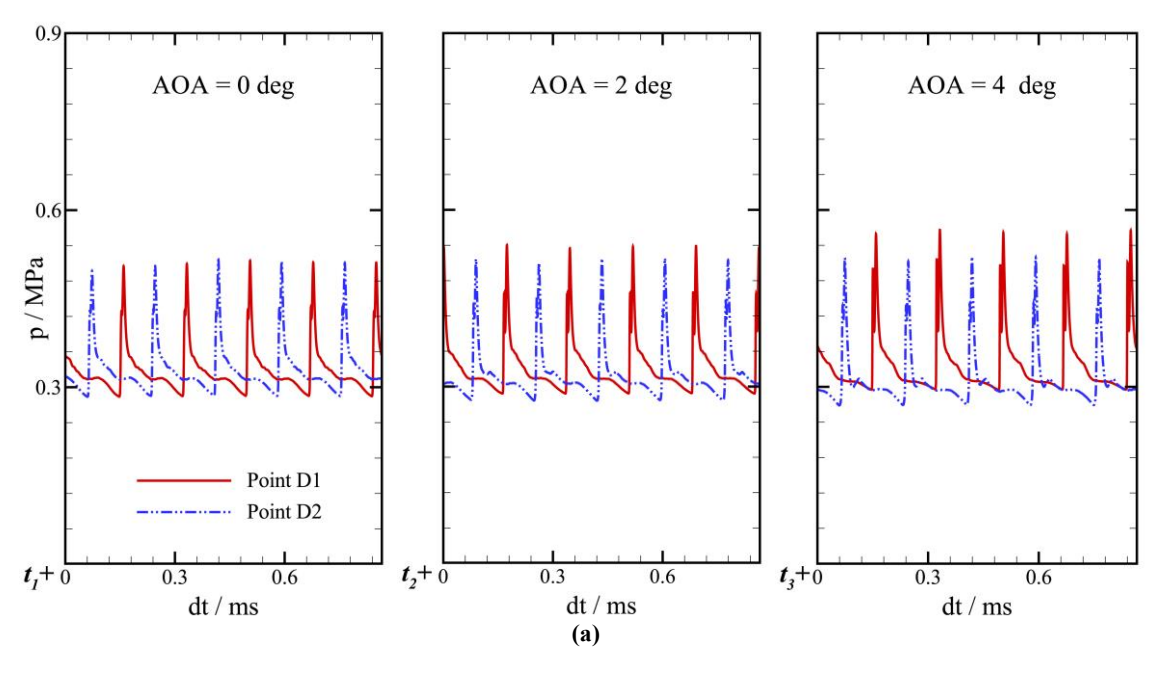


Fig 5. Transient pressure histories of different monitoring points upstream of the backward-facing step of the cavity in the hot-fire condition: (a) Point A1, A2; (b) Point B1, B2; (c) Point C1,

As plotted in Fig.6, the rest monitoring points downstream of the cavity forewall are captured to investigate the movement of detonation waves, induced shock waves, and shear layers. Here, points D1 and D2 are located at the middle of the cavity; points E1 and E2 are placed at the cavity aft lip; points F1 and F2 are fixed in the straight channel. The pressure variations of points D1 and D2 are separately enlarged by 17.4% and 24.2% with the attack angle rising from 0° to 4°. In contrast with Fig.5 (c), the drop of peak pressure in Fig.6 (a)-(c) mainly comes from the sudden expansion at the cavity forewall. The pressure variations of points D1, E1, and F1 with respect to the attack angle are quite similar, having positive correlations to their peak pressure. Meanwhile, the pressure troughs of points D1, E1, and F1 remain almost unchanged at different attack angles, of which the average values are 0.291 MPa, 0.245 MPa, and 0.202 MPa, respectively. Different from point D2, the pressure variations of points E2 and F2 decrease by 13.5% and 25.4% with the increase in the attack angle, indicating that the further lateral expansion of the aerodynamic diverging channel formed by the shear layer and the injection plane dampens the flow fluctuations.



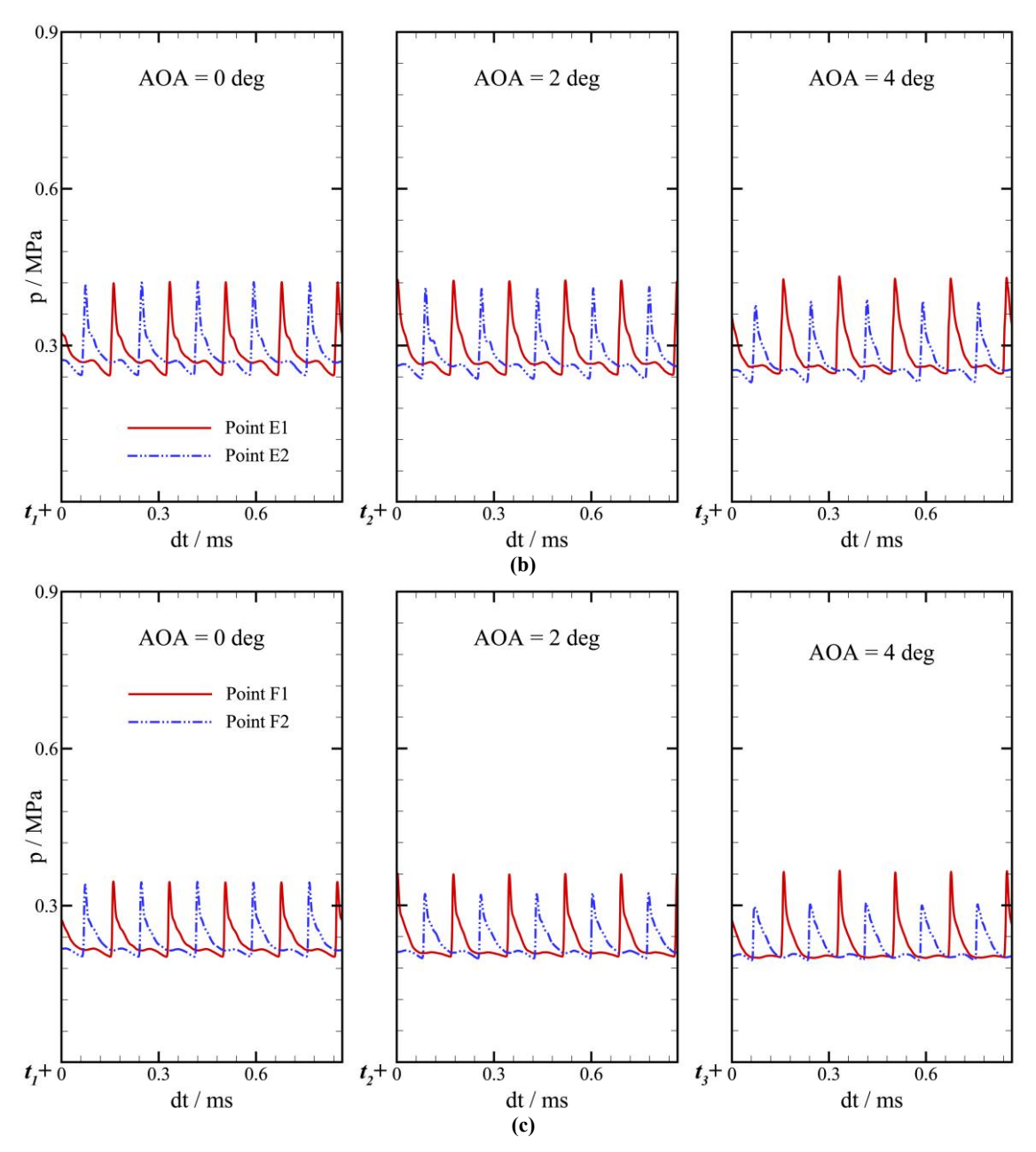


Fig 6. Transient pressure histories of different monitoring points downstream of the forward-facing step of the cavity in the hot-fire condition: (a) Point D1, D2; (b) Point E1, E2; (c) Point F1, F2.

In order to show the effects of attack angle on the flow states over a long time duration, the time-averaged pressure distributions of the leeward and windward sides along the mainstream direction are displayed in Fig.7. In general, the average pressure nondimensionalized by the ambient pressure first rises and then decreases. The maximum pressure ratio is located at the cavity forewall (x = 260 mm), and the pressure decaying process in the cavity is flat at first and then steep. The underlying reason is that the sudden expansion caused by the cavity geometry is delayed by the recirculation zone close to the cavity. In contrast with the static pressurization by the isolator, the static pressurization by the fuel combustion is almost two times. Upstream of the middle of the cavity, the pressure ratio is positively correlated with the attack angle on the leeward side. When the flow enters the straight channel, the pressure ratio on the leeward side is negatively related to the attack angle. This transformation comes from the lateral expansion effects that surpass the shock strength enhancement on the leeward side. As for the windward side, the overpressure exerted on the fuel injectors degenerates the static pressure rise in the cavity. With the increase in the attack angle, the average pressure ratios from the isolator end to the straight channel integrally decrease, originating from the joint action of the detonation

strength attenuation and the augmented flow loss of shock waves and viscous effects. Quantitatively, due to the nonuniform inflow, the pressure ratio increases by only 1.9% on the leeward side, but decreases by 5.2% on the windward side at the detonation foot. The limited aerodynamic parameter increment created by the leeward side at a nonzero attack angle is compactly restricted between the isolator end and the middle of the cavity, but the decrement created by the windward side is much more obvious in the whole flowpath. Therefore, the deteriorated performance caused by the nonzero attack angle is inevitable, though the detonation brings some benefits to the thermal efficiency.

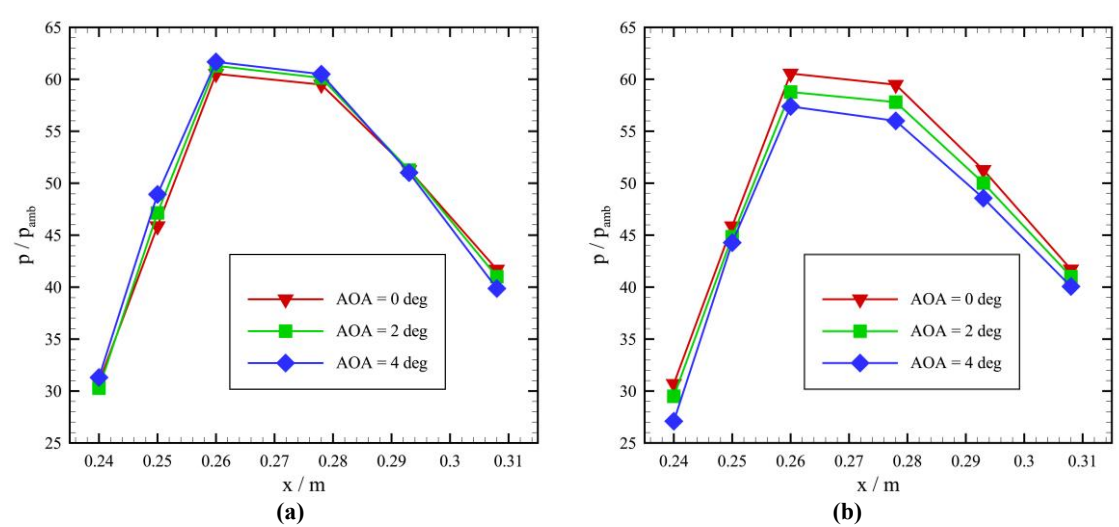


Fig 7. Time-averaged pressure ratios from the isolator end to the combustor exit in the axial direction: (a) Leeward: (b) Windward.

As listed in Tab. 2, the performance parameters at the design point provide an extra insight into the coupling effects among the engine components. Here, RMSD₀, defined as the root-mean-square deviation of the flow angle from the axis, is equal to 6.57°, revealing that the flow fluctuations are moderate. Machexit is close to one, indicating that a nozzle converging section is unnecessary. The total temperature increment reaches 1503 K, implying the superiority of detonation in energy addition to the high-speed mainstream. In addition, the mass flow rate captured by the inlet is 0.52 kg·s⁻¹, tightly related to the magnitude of the axial thrust.

Parameters	Values
RMSD ₀ , °	6.57
Mach _{exit}	1.04
ΔT _t , K	1503
<i>т</i> і, kg·s ⁻¹	0.52

Table 2. Performance parameters at the design point

5. Conclusions

It is numerically demonstrated that a non-premixed ethylene-fueled continuous detonation ramjet can operate steadily at the flight Mach number of five in the flight height of 20 km at the level flight state. The calculated model reaches a mass flow rate of 0.52 kg·s⁻¹ at a working frequency of 5787 Hz. It is found that the combination of a diverging isolator and a cavity-based combustor is an effective way to dampen the flow disturbances caused by the periodically sweeping shock waves, and the design methods for the steady flow can still be applied to the inlets and the nozzles in RDEs to some extent.

Acknowledgements

We would like to acknowledge the supports of Key Laboratory of Inlet and Exhaust System Technology at the Ministry of Education (CEPE2024011), Jiangsu Funding Program for Excellent Postdoctoral Talent (2024ZB332), and National Science Foundation of China (No.12332018 and No.12402389). We are also grateful to the organizers of this grant event.

References

1. Rankin, B.A., Fotia, M.L., Naples, A.G., Stevens, C.A., Hoke, J.L., Kaemming, T.A., Theuerkauf, S.W., Schauer, F.R.: Overview of performance, application, and analysis of Rotating detonation engine technologies. J. Propuls. Power 33 (1), 131-143 (2017).

https://doi.org/10.2514/1.B36303

2. Lu, F.K., Braun, E.M.: Rotating detonation wave propulsion: experimental challenges, modeling, and engine concepts. J. Propuls. Power 30 (5), 1125-1142 (2014).

https://doi.org/10.2514/1.B34802

3. Anand, V., Gutmark, E.: Rotating detonations and spinning detonations: similarities and differences. AIAA J. 56 (5), 1717-1722 (2018).

https://doi.org/10.2514/1.J056892

4. Kailasanath, K., Schwer, D.A.: High-fidelity simulations of pressure-gain combustion devices based on detonations. J. Propuls. Power 33 (1), 153-162 (2017).

https://doi.org/10.2514/1.B36169

- 5. Wolanski, P.: RDE research and development in Poland. Shock Waves 31, 623-636 (2021). https://doi.org/10.1007/s00193-021-01038-2
- 6. Braun, E.M., Lu, F.K., Wilson, D.R., Camberos, J.A.: Airbreathing rotating detonation wave engine cycle analysis. Aerosp. Sci. Technol. 27, 201-208 (2013).

https://doi.org/10.1016/j.ast.2012.08.010

7. Ivanov, V.S., Frolov, S.M., Zangiev, A.E., Zvegintsev, V.I., Shamshin, I.O.: Hydrogen fueled detonation ramjet: conceptual design and test fires at Mach 1.5 and 2.0. Aerosp. Sci. Technol. 109, 106459 (2021).

https://doi.org/j.ast.2020.106459

8. Frolov, S.M., Zvegintsev, V.I., Ivanov, V.S., Aksenov, V.S., Shamshin, I.O., Vnuchkov, D.A., Nalivaicheko, D.G., Berlin, A.A., Fomin, V.M.: Continuous detonation combustion of hydrogen: results of wind tunnel experiments. Combust. Explos. Shock Waves 54, 357-363 (2018).

https://doi.org/10.1134/S0010508218030139

9. Dubroskii, A.V., Ivanov, V.S., Zangiev, A.E., Frolov, S.M.: Three-dimensional numerical simulation of the characteristics of a ramiet power plant with a continuous-detonation combustor in supersonic flight. Rus. J. Phys. Chem. B 10(3), 469-482 (2016).

https://doi.org/10.1134/S1990793116030179

10. Katta, V.R., Cho, K.Y., Hoke, J.L., Codoni, J.R., Schauer, F.R., Roquemore, W.M.: Effect of increasing channel width on the structure of rotating detonation wave. Proc. Combust. Inst. 37(2), 3575-3583 (2019).

https://doi.org/10.1016/j.proci.2018.05.072

11. Kwasaki, A., Inakawa, T., Kasahara, J., Goto, K., Matsuoka, K., Matsuo, A., Funaki, I.: Critical condition of inner cylinder radius for sustaining rotating detonation waves in rotating detonation engine thruster. Proc. Combust. Inst. 37(3), 3461-3469 (2019).

https://doi.org/10.1016/j.proci.2018.07.070

12. Xia, Z., Tang, X., Luan, M., Zhang, S., Ma, Z., Wang, J.: Numerical investigation of two-wave collision and wave structure evolution of rotating detonation engine with hollow combustor. Int. J. Hydrog. Energy 43, 21582-21591 (2018).

https://doi.org/10.1016/j.ijhydene.2018.09.165

- 13. Liu, X., Chen, Y., Xia, Z., Wang, J.: Numerical study of the reverse-rotating waves in a rotating detonation engine with a hollow combustor. Acta Astronaut. 170, 421-430 (2020). https://doi.org/j.actaastro.2020.02.008
- 14. Peng, H., Liu, S., Liu, W., Yuan, X., Cai, X.: Enhancement of ethylene-air continuous rotating detonation in the cavity-based annular combustor. Aerosp. Sci. Technol. 115, 106842 (2021). https://doi.org/10.1016/j.ast.2021.106842
- 15. Wang, G., Liu, W., Liu, S., Zhang, H., Peng, H., Zhou, Y.: Experimental verification of cylindrical air-breathing continuous rotating detonation engine fueled by non-premixed ethylene. Acta Astronaut. 189, 722-732 (2021).
 - https://doi.org/10.1016/j.actaastro.2021.09.009
- 16. Li, Q., Liu, P., Zhang, H.: Further investigations on the interface instability between fresh injections and burnt products in 2-D rotating detonation. Comput. Fluids 170, 261-272 (2018). https://doi.org/j.compfluid.2018.05.005
- Sun, J., Zhou, J., Liu, S., Lin, Z., Lin, W.: Numerical investigation of a non-premixed hollow rotating detonation engine. Int. J. Hydrog. Energy 44, 17084-17094 (2019). https://doi.org/10.1016/j.ijhydene.2019.04.168